

High-Temperature Strong Nonreciprocal Thermal Radiation from Semiconductors

Bardia Nabavi, Sina Jafari Ghalekohneh, Komron J. Shayegan, Eric J. Tervo, Harry Atwater, and Bo Zhao*



Cite This: *ACS Photonics* 2025, 12, 2767–2774



Read Online

ACCESS |

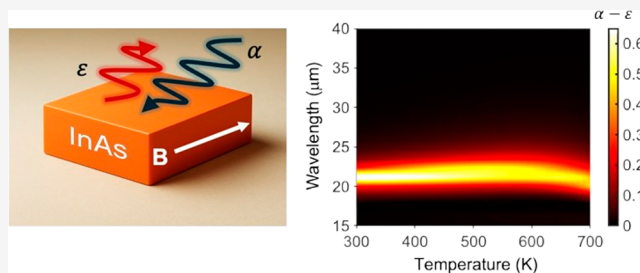
Metrics & More

Article Recommendations

Supporting Information

ABSTRACT: Nonreciprocal thermal emitters that break the conventional Kirchhoff's law allow independent control of emissivity and absorptivity and promise exciting new functionalities in controlling heat flow for thermal and energy applications. In enabling some of these applications, nonreciprocal thermal emitters will unavoidably need to serve as hot emitters. Leveraging magneto-optical effects, degenerate semiconductors have been demonstrated as a promising optical material platform for nonreciprocal thermal radiation. However, existing modeling and experimental efforts are limited to near room temperature (<373 K), and it remains unclear whether nonreciprocal properties can persist at high temperatures. In this work, we demonstrate strong nonreciprocal radiative properties at temperatures up to 600 K. We propose a theoretical model by considering the temperature dependence of the key parameters for the nonreciprocal behavior and experimentally investigate the temperature dependence of the nonreciprocal properties of sufficiently doped InAs, a degenerate semiconductor, using a customized angle-resolved high-temperature magnetic emissometry setup. Our theoretical model and experimental results show agreement, revealing that strong nonreciprocity can persist at temperatures over 800 K for high-temperature stable semiconductors, enabling a pathway for nonreciprocal radiative heat flow control at high temperatures.

KEYWORDS: nonreciprocity, thermal radiation, semiconductors, high-temperature properties, radiative heat transfer, emissometry



INTRODUCTION

Recent decades have witnessed remarkable advances in thermal radiation control through engineered nanophotonic structures.^{1,2} Beyond controlling thermal radiation with subwavelength structuring, integration of nonreciprocal materials into photonically engineered thermal emitters has emerged as a new route to unequal emissivity and absorptivity properties, due to the breaking of Lorentz reciprocity.^{2–5} Through magneto-optic effects,^{2–5} nonlinear responses,⁶ or dynamic time modulation,^{7,8} nonreciprocal systems enable independent control of emissivity and absorptivity. The ability to control radiative properties promises novel functionalities for heat flow control^{5,9} and energy harvesting.^{10–13}

Using magneto-optical materials among other approaches to achieve nonreciprocity has been explored in photonics for many years.¹⁴ These materials are typically semiconductors that support nonreciprocal response induced by the cyclotron motion of free electrons.¹⁵ Since early theoretical studies, advances have been made in achieving nonreciprocal thermal radiative properties leveraging the nonreciprocal responses in these materials.^{1,5,16} For example, Shayegan et al.^{17,18} experimentally demonstrated the inequality between emissivity and absorptivity of *n*-doped indium arsenide (InAs) planar and grating structures. Liu et al.¹⁹ achieved highly asymmetric

nonreciprocal absorption across a broadband long-wave infrared range (20–35 μm) using 14 InAs layers with gradient doping concentrations corresponding to cascaded epsilon-near-zero (ENZ) frequencies. A similar effect can be observed in other semiconductor and magnetic Weyl semimetal systems, as discussed in refs 17 and 18. Recently, Do et al.²⁰ used Bayesian optimization and designed a multilayer InAs and magnetic Weyl semimetal hybrid structure with only a few layers that can achieve strong nonreciprocal emission from 5 to 40 μm, highlighting the great potential for semiconductors in achieving nonreciprocal thermal emission.

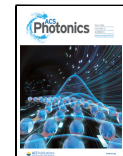
In enabling functionalities associated with radiative heat flow control, nonreciprocal thermal emitters that can sustain high temperatures are critical.¹¹ It is expected that semiconductor properties, such as free carrier concentration, exhibit a strong temperature dependence.^{17,21} While significant progress has been made in experiments, most studies have focused on near-

Received: February 14, 2025

Revised: April 21, 2025

Accepted: April 23, 2025

Published: April 30, 2025



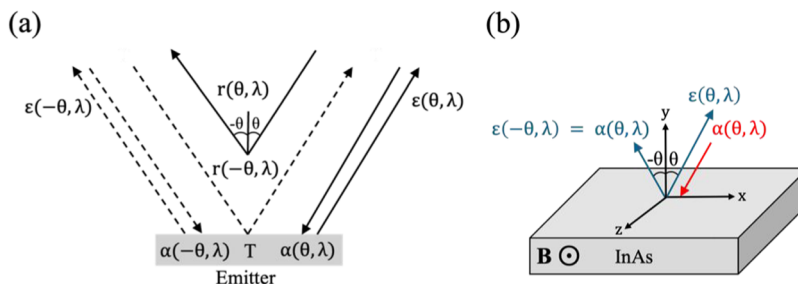


Figure 1. (a) Schematic of radiative heat transfer paths for a thermal emitter with specular reflection. Solid and dashed arrows show the energy flow balance for beams incident from the $+θ$ or $-θ$ directions, respectively. (b) Illustration of the InAs structure considered in this work.

room temperatures, with experimental conditions rarely exceeding 423 K,¹⁷ below which the intrinsic carrier concentration is negligible compared to extrinsic carriers in degenerate samples.^{21,22} As temperatures go well above room temperature, the change in carrier concentration,²¹ effective electron mass,^{21,22} high-frequency permittivity,²³ and electron mobility²⁴ becomes non-negligible. However, it is not clear how these material property changes could impact the nonreciprocal properties.

In this work, we investigate the high-temperature nonreciprocal thermal radiative properties from semiconductors. We propose a model for the dielectric functions of the semiconductors by considering the temperature dependence of material parameters relevant to nonreciprocity. As a verification of the model, we measure the temperature-dependent, nonreciprocal radiative properties of two InAs samples with different doping using an in-house developed, angle-resolved, high-temperature magnetic emissometry setup. We show that, despite a decrease in nonreciprocal contrast between emissivity and absorptivity, a strong nonreciprocal effect persists even at temperatures over 600 K.

THEORETICAL MODEL

The nonreciprocal thermal radiative properties are characterized by the imbalance between the directional spectral emissivity (ϵ) and absorptivity (α) as illustrated in Figure 1a. These properties can be computed from scattering properties such as reflectivity (r). Here, we consider opaque planar nonreciprocal thermal emitters, as depicted in Figure 1b. These emitters possess a specular reflection, and the emissivity and absorptivity can be obtained as^{25,26}

$$\epsilon(\theta, \lambda) = 1 - r(-\theta, \lambda) \quad (1)$$

$$\alpha(-\theta, \lambda) = 1 - r(\theta, \lambda) \quad (2)$$

where r can be computed by solving Maxwell's equations at the interface. In this study, we use an in-house developed²⁷ nonreciprocal rigorous coupled-wave analysis algorithm.²⁷ The level of nonreciprocity in radiative properties can be evaluated using the contrast between absorptivity and emissivity, expressed as

$$\eta(\theta, \lambda) = |\alpha(\theta, \lambda) - \epsilon(\theta, \lambda)| \quad (3)$$

The nonreciprocal radiative properties result from the nonreciprocal dielectric tensor by the magneto-optical behavior of semiconductors in a magnetic field. In general, when the magnetic field (B-field) is applied along the z direction, the temperature-dependent dielectric tensor can be described with a Drude model as^{4,28,29}

$$\epsilon = \begin{bmatrix} \epsilon_{xx} & \epsilon_{xy} & 0 \\ \epsilon_{yx} & \epsilon_{yy} & 0 \\ 0 & 0 & \epsilon_{zz} \end{bmatrix} \quad (4)$$

$$\epsilon_{xx} = \epsilon_{yy} = \epsilon_{\infty} - \frac{\omega_p^2(T)(\omega + i\gamma(T))}{\omega[(\omega + i\gamma(T))^2 - \omega_c^2(T)]} \quad (5)$$

$$\epsilon_{xy} = -\epsilon_{yx} = i \frac{\omega_p^2(T)\omega_c(T)}{\omega[(\omega + i\gamma(T))^2 - \omega_c^2(T)]} \quad (6)$$

$$\epsilon_{zz} = \epsilon_{\infty} - \frac{\omega_p^2(T)}{\omega(\omega + i\gamma(T))} \quad (7)$$

where ϵ_{∞} is high-frequency relative permittivity, γ is electron scattering rate, ω is angular frequency, ω_c is cyclotron frequency defined as $\omega_c = eB/m^*$, where e is the elementary charge, B is magnetic field density, T is temperature, and m^* is effective electron mass.^{4,28,29} $\omega_p = \sqrt{n\epsilon_0/m^*}$ is plasma frequency where n is free carrier concentration and ϵ_0 is vacuum permittivity.^{4,28,29} Most of the parameters, as indicated in the above equations, are prone to change with varying temperature, T .²⁷ The key to modeling the nonreciprocal properties, therefore, relies on capturing the temperature dependence of these parameters. Here, we use *n*-doped InAs as shown in Figure 1b as an example to illustrate our model. With the dielectric tensor discussed above, such a system supports nonreciprocal responses for the transverse magnetic (TM) polarization (with the magnetic field along the z -direction). Other semiconductors can be modeled using a similar procedure using different parameters or equations for the material,^{30–32} and we detail the process in the Supporting Information.

The plasma frequency, which approximately determines the frequency of large nonreciprocal behavior, depends on both the free carrier concentration and the electron effective mass. The temperature dependence of the free carrier concentration is mainly caused by changes in band gap and effective density of states of both the conduction and valence bands:^{21,33}

$$E_g = E_{g0} - \frac{aT^2}{T + b} \quad (8)$$

$$N_c = 1.68 \times 10^{13} T^{1.5} \quad (9)$$

$$N_v = 1.27 \times 10^{15} T^{1.5} \quad (10)$$

$$n_i = \sqrt{N_c N_v} e^{-E_g/2kT} \quad (11)$$

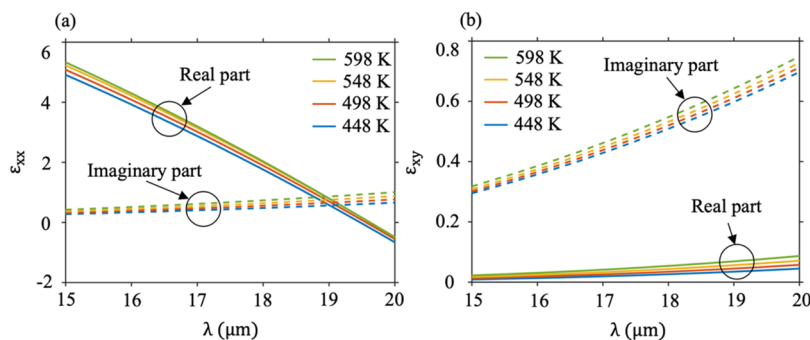


Figure 2. Real and imaginary parts of (a) ϵ_{xx} and (b) ϵ_{xy} as a function of wavelength λ for n -doped InAs with doping level of $1.4 \times 10^{18} \text{ cm}^{-3}$ at different temperatures.

$$n = N_D + \frac{n_i^2}{N_D} \quad (12)$$

where E_g is the band gap, E_{g0} , a , and b are 0.415 eV, 2.76×10^{-4} eV/K, and 83 K, respectively.^{33,34} N_c and N_v are effective densities of states in the conduction and valence bands, respectively, k is the Boltzmann constant, n_i is the intrinsic carrier concentration, N_D is doping level, and T is the absolute temperature. Equations 9 and 10 capture the main effect of a changing temperature on N_c and N_v ,³⁵ with the higher-order effect of changing effective mass neglected. Furthermore, we note that the temperature effect on carrier concentration is very mild for temperatures below 500 K for n-doped samples with a doping level lower than 10^{16} cm^{-3} .²¹ In this region, which is called the extrinsic region, the majority of free carriers come from dopants and the thermally excited carriers are negligible.²¹ The change in free carrier concentration impacts the dielectric function negligibly in this regime, which might seem counterintuitive.

The temperature threshold up to which the impact on the carrier concentration of the semiconductor can be neglected depends largely on the band gap and the doping level.²¹ For larger band gap semiconductors, for example, gallium arsenide (GaAs), the carrier concentration does not change significantly up to 600 K for doping levels of 10^{18} cm^{-3} , as shown in the Supporting Information.

The effective electron mass is influenced by temperature through its dependence on the band gap:^{36,37}

$$\frac{m^*}{m_e} = 0.0310 - 0.0218E_g + 0.1E_g^2 - 0.046E_g^3 \quad (13)$$

where m_e is the free electron mass. Decreasing band gap with increasing temperature reduces the effective mass at higher temperatures, thereby increasing the cyclotron frequency for a given magnetic field. Therefore, the change in effective mass contributes a stronger nonreciprocal effect at higher temperature.

Additionally, the scattering rate varies with temperature. We determine the temperature effect on the electron scattering rate using a widely used empirical model for low-field mobility:²⁴

$$\mu_{LF}(n, T) = \mu_{\min} + \frac{\mu_{\max} \left(\frac{380}{T} \right)^{\psi_1} - \mu_{\min}}{1 + \left(\frac{n}{n_{ref} \left(\frac{T}{300} \right)^{\psi_2}} \right)^{\zeta}} \quad (14)$$

where n_{ref} is reference doping concentration $1.1 \times 10^{18} \text{ cm}^{-3}$, μ_{\max} is mobility at 300 K, and μ_{\min} is the minimum mobility. The respective mobility values are 34,000 and $1000 \text{ cm}^2/\text{V}\cdot\text{s}$ for n -doped InAs.²⁴ The experimentally determined ψ_1 , ψ_2 , and ζ ²⁴ are 1.57, 3, and 0.32, respectively. The electron scattering rate can be derived from the electron mobility as follows:³⁵

$$\gamma = \frac{q}{\mu_{LF} m^*} \quad (15)$$

where q is the elementary charge. As shown in the Supporting Information, an increase in temperature causes an increase in electron scattering.

Besides the parameters describing free electrons in a semiconductor, previous research indicate that the high-frequency relative permittivity ϵ_∞ also varies with temperature.²³ The importance of this dependence has been noted in ref 15, and it directly impacts the spectral location of the ENZ region at different temperatures. Based on the tabulated data from ref 21, we derive a linear model using least-squares regression to capture this dependence:

$$\epsilon_\infty = \delta T + \sigma \quad (16)$$

Here, δ and σ are 0.0018 K^{-1} and 13.54, respectively. The positive high-frequency permittivity competes with the negative Drude term, which determines the spectral location of the ENZ region. As temperature increases, the high-frequency permittivity increases, causing a redshift of the ENZ region.

The overall temperature dependence arises from the collective contributions of all the above-mentioned parameters. Among these, the scattering rate and high frequency permittivity cause significant changes in permittivity as the temperature varies, which is confirmed by calculating the permittivity of the material at high temperatures while keeping all other parameters constant. In the Supporting Information, we present the temperature dependence of all parameters for two representative magneto-optical materials: InAs and GaAs and their stoichiometric combination, $\text{In}_{0.53}\text{Ga}_{0.47}\text{As}$. Figure 2 illustrates the temperature dependence of the diagonal and off-diagonal dielectric function for InAs based on our model. It is interesting to note that the imaginary part of the off-diagonal component ϵ_{xy} increases with rising temperature. However, it does not necessarily imply an increased nonreciprocal effect since the diagonal term of permittivity ϵ_{xx} and the scattering of the material also increase. In fact, as shown in the following, the nonreciprocal effect generally decreases as temperature increases. The shift of the real part of ϵ_{xx} causes a notable redshift of the ENZ region.

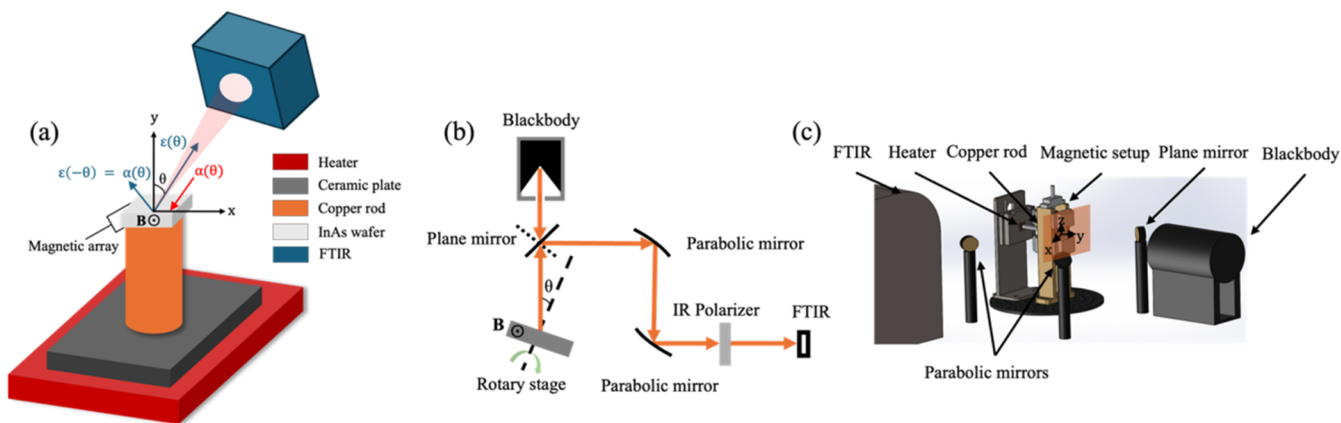


Figure 3. Schematic of the emissometry setup. (a) A ceramic heater ensures uniform heating. A copper rod guides the heat to the sample, which is attached to the end of the rod. An array of magnets surrounds the sample, providing the external magnetic field. The emission is detected by the FTIR to measure the emissivity of the samples. (b) The beam path of the emissometry setup. (c) Schematic of the emissometry setup showing the arrangement of all parts.

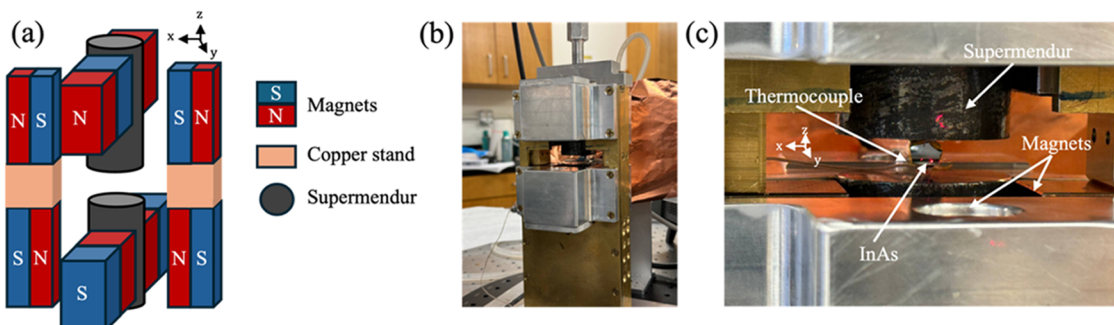


Figure 4. Schematic of the magnet assembly. (a) N and S represent the north and south poles of the permanent magnets. Eight neodymium magnets are arranged surrounding the supermendur, providing a magnetic field as high as 1 T. Magnets and supermendur are mounted on a copper stand. (b) Picture of the copper stand of the magnetic assembly and stainless-steel fixture. (c) Picture of the sample in the magnetic field. Thick copper foil with a round hole for the fin structure is used to block radiation coming from the sample stage.

■ EXPERIMENTAL MEASUREMENT SETUP

We conduct an experimental demonstration of the radiative properties of single crystal *n*-doped InAs samples as a verification of our model. We develop a high-temperature angle-resolved magnetic emissometry setup for this purpose, as shown in Figure 3. Samples are mounted on a sample stage, which is a PID-controlled ceramic heater (Instec Inc. model number HS1200G). The sample stage is placed on a freely rotatable plate, allowing for changes in the emission direction. The emitted radiation from the sample is directed through a plane gold mirror and two parabolic gold mirrors to a Fourier Transform Infrared (FTIR) spectroscopy system, where a zinc selenide (ZnSe) polarizer can be added to the beam path. The plane mirror can be reconfigured to guide the emission from a blackbody source, enabling spectral measurements of the reference blackbody at the same temperature as the sample. The spectral directional emissivity of the sample can then be measured as³⁸

$$\varepsilon(\lambda, \theta, B, T_s) = \varepsilon_R(\lambda) \frac{I_S(\lambda, \theta, B, T_s) - I_{BG}(\lambda, \theta, T_s)}{I_R(\lambda, T_s) - I_{BG}(\lambda, \theta, T_s)} \quad (17)$$

where B is magnetic field density, and T_s is temperature of the sample. I_S , I_R , and I_{BG} refer to measured spectral intensity from the sample, the reference blackbody, and the background, respectively. The emissivity of the reference material, ε_R is the

emissivity of a blackbody and equal to one for all wavelengths in our measurements. A thick copper foil is used to cover the sample stage to block the radiation from the other parts of the sample stage, reducing the background emission as much as possible. To quantify the remaining spectral intensity of the background, a thin aluminum foil of the same area as the sample is attached at the tip of the rod to replace the sample, and the intensity is recorded at the same temperature as the InAs samples. From eqs 1 and 2, one can see that $\varepsilon(\theta, \lambda) = \alpha(-\theta, \lambda)$. Therefore, the absorptivity at $-\theta$ can be obtained from the emissivity at angle θ , providing an approach to obtain the absorptivity directly from the emission measurement. We use this approach in our experiment to obtain the absorptivity, emissivity, and the nonreciprocal contrast of InAs.

To induce the nonreciprocal response, a magnetic field is required. Here, the external magnetic field is applied to the sample via a magnetic assembly placed on the rotary stage. The design of the magnetic setup is shown in Figure 4. Inspired by,³⁹ we place four pairs of neodymium (NdFeB) magnets to enhance the magnetic field strength between two supermendur rods. In doing so, a B-field up to 1 T can be achieved in the 1 cm gap between the two supermendur rods, where the sample can be placed.

We note that the fin structure introduced in the sample stage is a key difference as compared to the temperature-controlled sample stage in traditional emissometry systems.⁴⁰ Here, we

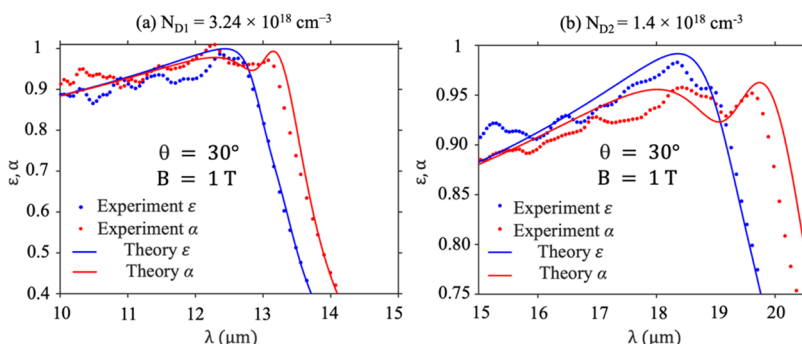


Figure 5. Radiative properties for p -polarized waves as a function of wavelength λ for n -doped InAs samples with different doping levels at 598 K. (a) Experimental and theoretical results for the InAs sample with $N_{D1} = 3.24 \times 10^{18} \text{ cm}^{-3}$. (b) Experimental and theoretical absorptivity results for the InAs sample with $N_{D2} = 1.4 \times 10^{18} \text{ cm}^{-3}$.

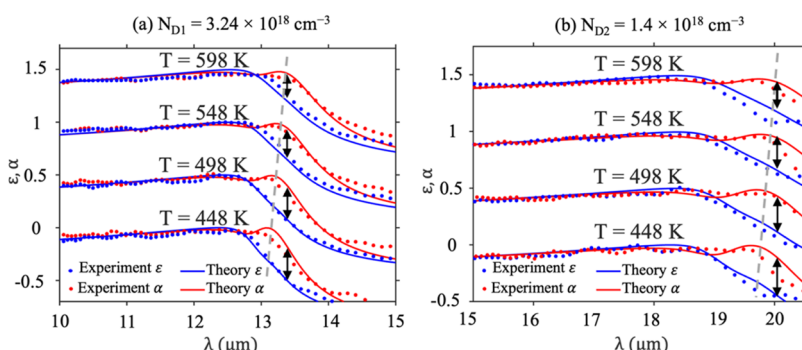


Figure 6. Absorptivity and emissivity measurements and calculations at different temperatures at $\theta = 30^\circ$. These results are shifted by 0.5. (a) The sample with $N_{D1} = 3.24 \times 10^{18} \text{ cm}^{-3}$. (b) The sample with $N_{D2} = 1.4 \times 10^{18} \text{ cm}^{-3}$. Arrows are added to better visualize the contrast change at the same wavelength. Dashed lines show the redshift for higher temperatures.

use a fin structure with one end of the fin in contact with the ceramic heater to guide the heat flow to the sample that is placed on the other end of the fin. In doing so, we can elevate the sample from the heating stage, allowing enough space for the magnetic assembly, as indicated in Figure 3c. A K-series thermocouple is positioned at the tip of the rod near the sample to monitor the temperature of the sample. Despite the heat loss induced by the introduction of the fin structure, we are still able to achieve sample temperatures of up to about 1000 K.

RESULTS AND DISCUSSION

Figure 5a and b show the measured emissivity and absorptivity spectra for TM polarizations at $T = 598 \text{ K}$, $\theta = 30^\circ$, and $B = 1 \text{ T}$ for two InAs samples with different doping levels of $N_{D1} = 3.24 \times 10^{18} \text{ cm}^{-3}$ (sample 1) and $N_{D2} = 1.4 \times 10^{18} \text{ cm}^{-3}$ (sample 2), respectively. Both samples are $525 \mu\text{m}$ thick and can be considered as opaque in the mid-infrared wavelength range. The theoretical results based on the developed model are also overlaid, agreeing well with the experiment. For sample 2, the spectra exhibit a prominent peak around $20 \mu\text{m}$, corresponding to the leaky Brewster mode^{41,42} in the ENZ region. The Brewster mode shifts to shorter wavelengths (about $13 \mu\text{m}$) for sample 1 due to the increase of the plasma frequency, as shown in Figure 5a.

The emissivity and absorptivity spectra show a significant difference, particularly near the region where the Brewster modes are excited. The difference clearly demonstrates the strong nonreciprocal response, which breaks the conventional Kirchhoff's law of thermal radiation at approximately 600 K.

We note that the enhancement of nonreciprocity by Brewster modes is even stronger at larger angles as shown in Figure S2 in the Supporting Information. We focus on investigating $\theta = 30^\circ$ to achieve a better signal-to-noise ratio in the experiment. The nonreciprocal contrast can be greater at larger angles.⁴³ As control experiments, we also conduct the same measurement for the TM polarization with $B = 0 \text{ T}$ and the TE polarization (electric field along the z direction). In both cases, we observe overlapping emissivity and absorptivity spectra with no contrast, obeying the conventional Kirchhoff's law of thermal radiation.^{44,45}

As we change the temperature, the nonreciprocal properties exhibit prominent change, as shown in Figure 6. Both samples are tested at three other different temperatures. As in Figure 5, the nonreciprocal behavior occurs in all cases. As temperature increases, the peak caused by the Brewster mode shifts slightly to longer wavelengths, which is more clearly observed from the absorptivity spectra for both samples. Since the plasma frequency tends to increase as a function of temperature as shown in Supporting Information, the shift of the Brewster mode is mainly caused by the increase of the ε_∞ as temperature increases, which results in the ENZ region occurring at slightly longer wavelengths.

Besides the shift of the Brewster modes, higher temperatures also bring a strong effect on the nonreciprocal contrast. In Figure 6, we mark the maximum contrast between ε and α with arrows. We first determine the maximum contrast near the Brewster mode and its corresponding wavelength based on the computed spectrum at $T = 598 \text{ K}$. Then we mark the contrast at the same wavelength for all temperatures with double-

headed arrows, clearly showcasing the decrease of the contrast at a fixed wavelength when temperature increases. Furthermore, dashed lines illustrate changes in the wavelength corresponding to the peak location of the Brewster modes for the absorptivity spectra. As another approach to illustrate the temperature effect on the contrast, Figure 7 shows the

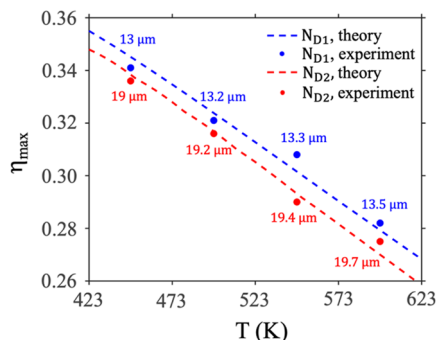


Figure 7. Maximum contrast between emissivity and absorptivity (η_{\max}) for *n*-doped InAs samples. N_{D1} and N_{D2} refer to the samples with carrier concentrations of 3.24×10^{18} and $1.4 \times 10^{18} \text{ cm}^{-3}$, respectively. The corresponding wavelengths at which the maximum contrast occurs are marked.

maximum contrast and the corresponding wavelength as a function of the temperature for both samples. Due to the shift of the Brewster modes, the wavelength at which the maximum contrast occurs also shifts to longer wavelengths as the temperature increases. Meanwhile, the maximum contrast gradually decreases as the temperature increases. This is primarily caused by the increase in the scattering rate, which also broadens the Brewster modes. Our proposed theoretical model captures both temperature effects well, demonstrating the effectiveness of the model.

The temperature-dependent nonreciprocal properties have several implications. So far, the design of nonreciprocal thermal emitters has been limited to room temperature or near room temperatures.^{17,19} These designs may need to be reexamined if one would apply them to high temperature applications. This also applies to magnetic Weyl semimetals, whose nonreciprocal properties could reduce significantly as temperature increases because of the sensitive temperature response near the Weyl cones, as discussed in ref 38. However, for semiconductors, our results reveal that the nonreciprocal response is still much more robust than Weyl semimetals against temperature change, which opens the possibility for high-temperature nonreciprocal thermal emission control.

In our study, we limit the sample temperature to 598 K since InAs could desorb when heated up to temperatures over 703 K.⁴⁶ The desorption temperature of semiconductors typically increases as the band gap increases.⁴⁷ For example, it has been experimentally demonstrated that gallium arsenide (GaAs) can be stable even up to about 800 K.^{48,49} Therefore, one could potentially utilize wider band gap materials for nonreciprocal thermal radiation control at even higher temperatures.

Motivated by these thoughts, we conduct a calculation based on our proposed theoretical model for $\text{In}_x\text{Ga}_{1-x}\text{As}$ semiconductors. In Figure 8, we show the nonreciprocal contrast for TM waves at $\theta = 80^\circ$ and $B = 1 \text{ T}$ for InAs, GaAs, and $\text{In}_{0.53}\text{Ga}_{0.47}\text{As}$, which can be readily grown on indium phosphide (InP).⁵⁰ In the calculations, we assume all materials are *n*-doped with the same doping level of $8.5 \times 10^{17} \text{ cm}^{-3}$. We choose a slightly lower doping level as compared to the previous InAs samples to highlight the fact that the high nonreciprocal contrast is not very sensitive to the change in doping levels. Strong nonreciprocity is observed for all material systems, with the contrast gradually decreasing with an increasing temperature. For GaAs, the contrast is not as strong as InAs due to its heavy electron mass.³⁷ The ENZ region also occurs at a longer wavelength range as indicated by the bright high-contrast band due to its larger band gap. The behavior of $\text{In}_{0.53}\text{Ga}_{0.47}\text{As}$ falls between InAs and GaAs in terms of wavelength and contrast values, indicating that the nonreciprocal properties can be tuned by varying x in the compound.²⁴ The results point the pathway for ultrahigh-temperature nonreciprocal thermal radiation.

While writing this manuscript, we were made aware of a work³⁸ that utilizes InGaAs for nonreciprocal thermal radiation at a temperature of 540 K. The results are consistent with our study, especially the results in Figures 8b and S2b in the Supporting Information.

CONCLUSIONS

In conclusion, this work demonstrates robust, high-temperature nonreciprocal thermal radiation in semiconductors, advancing the frontier of active radiative heat flow control. By developing a comprehensive theoretical model that accounts for temperature-dependent carrier dynamics, scattering rates, and permittivity shifts in magneto-optical materials, we successfully predicted and experimentally validated strong nonreciprocal contrasts in *n*-doped InAs at temperatures exceeding 600 K. Our customized angle-resolved magnetic emissometry setup revealed persistent nonreciprocity at elevated temperatures, with experimental results aligning closely with our theoretical predictions. The observed red-

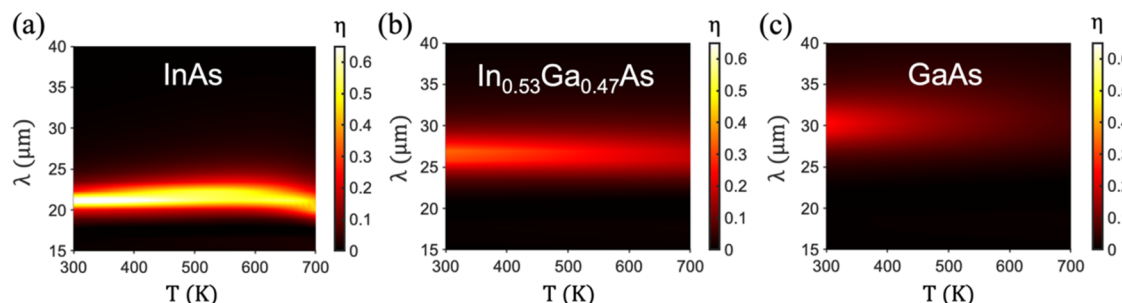


Figure 8. Contours for the nonreciprocal contrast as a function of temperature and wavelength for *n*-doped (a) InAs, (b) $\text{In}_{0.53}\text{Ga}_{0.47}\text{As}$, and (c) GaAs. All materials have the same doping level of $8.5 \times 10^{17} \text{ cm}^{-3}$.

shifting of epsilon-near-zero regions and moderated contrast reduction at higher temperatures highlight the resilience of semiconductor-based nonreciprocal emitters under thermal stress. We believe that wide-band gap semiconductors like GaAs could sustain nonreciprocal effects beyond 800 K, unlocking applications in high-temperature radiative heat flow control and energy harvesting. This study establishes a framework for designing temperature-robust nonreciprocal systems, bridging critical gaps in transitioning lab-scale demonstrations to real-world thermal management technologies.

ASSOCIATED CONTENT

Supporting Information

The Supporting Information is available free of charge at <https://pubs.acs.org/doi/10.1021/acsphtronics.5c00365>.

Theoretical model for GaAs; theoretical model for $In_{0.53}Ga_{0.47}As$; and angular dependence of the nonreciprocal behavior ([PDF](#))

AUTHOR INFORMATION

Corresponding Author

Bo Zhao – Department of Mechanical and Aerospace Engineering, University of Houston, Houston, Texas 77204, United States;  orcid.org/0000-0002-3648-6183; Email: bzhao8@uh.edu

Authors

Bardia Nabavi – Department of Mechanical and Aerospace Engineering, University of Houston, Houston, Texas 77204, United States;  orcid.org/0009-0004-8864-6152

Sina Jafari Ghalekohneh – Department of Mechanical and Aerospace Engineering, University of Houston, Houston, Texas 77204, United States

Komron J. Shayegan – Thomas J. Watson Laboratory of Applied Physics, California Institute of Technology, Pasadena, California 91125, United States; Department of Electrical Engineering, California Institute of Technology, Pasadena, California 91125, United States

Eric J. Tervo – Department of Electrical and Computer Engineering, University of Wisconsin-Madison, Madison, Wisconsin 53706, United States; Department of Mechanical Engineering, University of Wisconsin-Madison, Madison, Wisconsin 53706, United States;  orcid.org/0000-0002-8517-9649

Harry Atwater – Thomas J. Watson Laboratory of Applied Physics, California Institute of Technology, Pasadena, California 91125, United States; Department of Electrical Engineering, California Institute of Technology, Pasadena, California 91125, United States;  orcid.org/0000-0001-9435-0201

Complete contact information is available at:

<https://pubs.acs.org/10.1021/acsphtronics.5c00365>

Funding

University of Houston SEED program; National Science Foundation Grant No. CBET-2314210.

Notes

This study has been previously published through a preprint repository: High-Temperature Strong Nonreciprocal Thermal Radiation from Semiconductors. Nabavi, B.; S. Jafari Ghalekohneh, S.; Shayegan, K.J.; et al. High-Temperature

Strong Nonreciprocal Thermal Radiation from Semiconductors. 2025, 07245. arXiv preprint, doi.org/10.48550/arXiv.2502.07245 (Accessed February 11, 2025).

The authors declare no competing financial interest.

ACKNOWLEDGMENTS

The authors acknowledge the support of the Research Computing Data Core at the University of Houston for assistance with the calculations carried out in this work. B.N. and B.Z. thank Sahag Bozoian, Aniroodh Sivaraman, and Jamar Murray for their assistance in fabricating the magnetic assembly.

REFERENCES

- (1) Fan, S. Thermal photonics and energy applications. *Joule* **2017**, 1 (2), 264–273.
- (2) Zhu, L.; Guo, Y.; Fan, S. Theory of many-body radiative heat transfer without the constraint of reciprocity. *Phys. Rev. B* **2018**, 97 (9), No. 094302.
- (3) Snyder, W. C.; Wan, Z.; Li, X. Thermodynamic constraints on reflectance reciprocity and Kirchhoff's law. *Appl. Opt.* **1998**, 37 (16), 3464–3470.
- (4) Zhao, B.; Shi, Y.; Wang, J.; Zhao, Z.; Zhao, N.; Fan, S. Near-complete violation of Kirchhoff's law of thermal radiation with a 0.3T magnetic field. *Opt. Lett.* **2019**, 44 (17), 4203–4206.
- (5) Zhang, Z.; Zhu, L. Nonreciprocal thermal photonics for energy conversion and radiative heat transfer. *Phys. Rev. Appl.* **2022**, 18 (2), No. 027001.
- (6) Khandekar, C.; Pick, A.; Johnson, S. G.; Rodriguez, A. W. Radiative heat transfer in nonlinear Kerr media. *Phys. Rev. B* **2015**, 91 (11), No. 115406.
- (7) Ghanekar, A.; Wang, J.; Fan, S.; Povinelli, M. L. Violation of Kirchhoff's law of thermal radiation with space-time modulated grating. *ACS Photonics* **2022**, 9 (4), 1157–1164.
- (8) Hadad, Y.; Soric, J. C.; Alu, A. Breaking temporal symmetries for emission and absorption. *Proc. Natl. Acad. Sci. U.S.A.* **2016**, 113 (13), 3471–3475.
- (9) Fan, L.; Guo, Y.; Papadakis, G. T.; Zhao, B.; Zhao, Z.; Buddhiraju, S.; Orenstein, M.; Fan, S. Nonreciprocal radiative heat transfer between two planar bodies. *Phys. Rev. B* **2020**, 101 (8), No. 085407.
- (10) Park, Y.; Zhao, B.; Fan, S. Reaching the ultimate efficiency of solar energy harvesting with a nonreciprocal multijunction solar cell. *Nano Lett.* **2022**, 22 (1), 448–452.
- (11) Jafari Ghalekohneh, S.; Zhao, B. Nonreciprocal solar thermophotovoltaics. *Phys. Rev. Appl.* **2022**, 18 (3), No. 034083.
- (12) Park, Y.; Omair, Z.; Fan, S. Nonreciprocal thermophotovoltaic systems. *ACS Photonics* **2022**, 9 (12), 3943–3949.
- (13) Vázquez-Lozano, J. E.; Liberal, I. Review on the scientific and technological breakthroughs in thermal emission engineering. *ACS Appl. Opt. Mater.* **2024**, 2 (6), 898–927.
- (14) Bi, L.; Hu, J.; Jiang, P.; Kim, D. H.; Dionne, G. F.; Kimerling, L. C.; Ross, C. On-chip optical isolation in monolithically integrated non-reciprocal optical resonators. *Nat. Photonics* **2011**, 5 (12), 758–762.
- (15) Tanner, D. B. *Optical Effects in Solids*; Cambridge University Press, 2019; pp 25–59 DOI: [10.1017/9781316672778](https://doi.org/10.1017/9781316672778).
- (16) Fernandes, D. E.; Silveirinha, M. G. Enhancing the directional violation of Kirchhoff's law of thermal radiation with a nonreciprocal wire medium. *Phys. Rev. Appl.* **2023**, 20 (5), No. 054028.
- (17) Shayegan, K. J.; Biswas, S.; Zhao, B.; Fan, S.; Atwater, H. A. Direct observation of the violation of Kirchhoff's law of thermal radiation. *Nat. Photonics* **2023**, 17 (10), 891–896.
- (18) Shayegan, K. J.; Hwang, J. S.; Zhao, B.; Raman, A. P.; Atwater, H. A. Broadband nonreciprocal thermal emissivity and absorptivity. *Light: Sci. Appl.* **2024**, 13 (1), No. 176.

- (19) Liu, M.; Xia, S.; Wan, W.; Qin, J.; Li, H.; Zhao, C.; Bi, L.; Qiu, C.-W. Broadband mid-infrared non-reciprocal absorption using magnetized gradient epsilon-near-zero thin films. *Nat. Mater.* **2023**, *22* (10), 1196–1202.
- (20) Do, B.; Ghalekohneh, S. J.; Adebiyi, T.; Zhao, B.; Zhang, R. Automated design of nonreciprocal thermal emitters via Bayesian optimization. *J. Quant. Spectrosc. Radiat. Transfer* **2025**, *331*, No. 109260.
- (21) Pierret, R. F. *Semiconductor Device Fundamentals*; Addison-Wesley Publishing Company, 1996; pp 1–69.
- (22) Shayegan, K. J.; Zhao, B.; Kim, Y.; Fan, S.; Atwater, H. A. Nonreciprocal infrared absorption via resonant magneto-optical coupling to InAs. *Sci. Adv.* **2022**, *8* (18), No. eabm4308.
- (23) Degheidy, A. R.; Elkenany, E. B.; Madkour, M. A. K.; AbuAli, A. M. Temperature dependence of phonons and related crystal properties in InAs, InP and InSb zinc-blende binary compounds. *Comput. Condens. Matter* **2018**, *16*, No. e00308.
- (24) Sotoodeh, M.; Khalid, A.; Rezazadeh, A. Empirical low-field mobility model for III-V compounds applicable in device simulation codes. *J. Appl. Phys.* **2000**, *87* (6), 2890–2900.
- (25) Casimir, H. B. G. On Onsager's principle of microscopic reversibility. *Rev. Mod. Phys.* **1945**, *17* (2–3), 343.
- (26) Guo, C.; Zhao, B.; Fan, S. Adjoint Kirchhoff's law and general symmetry implications for all thermal emitters. *Phys. Rev. X* **2022**, *12* (2), No. 021023.
- (27) Yang, C.; Zhao, B.; Cai, W.; Zhang, Z. M. Mid-infrared broadband circular polarizer based on Weyl semimetals. *Opt. Express* **2022**, *30* (2), 3035–3046.
- (28) Zhu, L.; Fan, S. Near-complete violation of detailed balance in thermal radiation. *Phys. Rev. B* **2014**, *90* (22), No. 220301.
- (29) Madelung, O. *Semiconductors: Data Handbook*; Springer Science & Business Media, 2004; pp 397–419.
- (30) Paul, S.; Roy, J. B.; Basu, P. K. Empirical expressions for the alloy composition and temperature dependence of the band gap and intrinsic carrier density in $\text{Ga}_x\text{In}_{1-x}\text{As}$. *J. Appl. Phys.* **1991**, *69* (2), 827–829.
- (31) Zielinski, E.; Schweizer, H.; Streubel, K.; Eisele, H.; Weimann, G. Exciton transitions and exciton damping processes in InGaAs/InP. *J. Appl. Phys.* **1986**, *59* (6), 2196–2204.
- (32) Karachevtseva, M.; Ignat'ev, A.; Mokerov, V.; Nemtsev, G.; Strakhov, V.; Yaremenko, N. Temperature dependence of the photoluminescence of $\text{In}_x\text{Ga}_{1-x}\text{As}/\text{GaAs}$ quantum-well structures. *Semiconductors* **1994**, *28* (7), 691–694.
- (33) Varshni, Y. P. Temperature dependence of the energy gap in semiconductors. *Physica* **1967**, *34*, 149–154.
- (34) Fang, Z. M.; Ma, K.; Jaw, D.; Cohen, R.; Stringfellow, G. Photoluminescence of InSb, InAs, and InAsSb grown by organometallic vapor phase epitaxy. *J. Appl. Phys.* **1990**, *67* (11), 7034–7039.
- (35) Sze, S. M. *Semiconductor Devices: Physics and Technology*; John Wiley & Sons, 2008; pp 43–77.
- (36) Bouarissa, N.; Aourag, H. Effective masses of electrons and heavy holes in InAs, InSb, GaSb, GaAs and some of their ternary compounds. *Infrared Phys. Technol.* **1999**, *40*, 343–349.
- (37) Nakwaski, W. Effective masses of electrons and heavy holes in GaAs, InAs, AlAs and their ternary compounds. *Phys. B* **1995**, *210* (1), 1–25.
- (38) Zhang, Z.; Dehaghi, A. K.; Ghosh, P.; Zhu, L. Observation of Strong Nonreciprocal Thermal Emission. arXiv preprint arXiv:2501.12947 2025 DOI: [10.48550/arXiv.2501.12947](https://doi.org/10.48550/arXiv.2501.12947).
- (39) Adambukulam, C.; Sewani, V. K.; Stemp, H. G.; Asaad, S.; Mądzik, M. T.; Morello, A.; Laucht, A. An ultra-stable 1.5 T permanent magnet assembly for qubit experiments at cryogenic temperatures. *Rev. Sci. Instrum.* **2021**, *92* (8), No. 085106, DOI: [10.1063/5.0055318](https://doi.org/10.1063/5.0055318).
- (40) Shan, S.; Chen, C.; Loutzenhiser, P. G.; Ranjan, D.; Zhou, Z.; Zhang, Z. M. Spectral emittance measurements of micro/nanostructures in energy conversion: a review. *Front. Energy* **2020**, *14*, 482–509.
- (41) Taliercio, T.; Guilengui, V. N.; Cerutti, L.; Tournié, E.; Greffet, J.-J. Brewster mode in highly doped semiconductor layers: an all-optical technique to monitor doping concentration. *Opt. Express* **2014**, *22* (20), 24294–24303.
- (42) Jafari Ghalekohneh, S.; Du, C.; Zhao, B. Controlling the contrast between absorptivity and emissivity in nonreciprocal thermal emitters. *Appl. Phys. Lett.* **2024**, *124* (10), No. 101104, DOI: [10.1063/5.0187105](https://doi.org/10.1063/5.0187105).
- (43) Xu, Y.; Wang, B.; Ye, J. Near-infrared violation of Kirchhoff's law of thermal radiation at near-zero angle. *Int. J. Therm. Sci.* **2025**, *211*, No. 109752.
- (44) Liang, G.; Wang, B. Multi-channel nonreciprocal radiation of transverse electric wave with photonic crystal heterostructure. *Appl. Phys. Lett.* **2024**, *125* (21), No. 212202, DOI: [10.1063/5.0238096](https://doi.org/10.1063/5.0238096).
- (45) Shi, X.; Wang, B. Dual-polarization strong nonreciprocal radiation by the 2D GaAs nanograting. *Appl. Phys. Lett.* **2024**, *125* (6), No. 062202, DOI: [10.1063/5.0225127](https://doi.org/10.1063/5.0225127).
- (46) Yamaguchi, H.; Horikoshi, Y. As desorption from GaAs and AlAs surfaces studied by improved high-energy electron reflectivity measurements. *J. Appl. Phys.* **1992**, *71* (4), 1753–1759.
- (47) Laughlin, D.; Wilmsen, C. Thermal oxidation of InAs. *Thin Solid Films* **1980**, *70* (2), 325–332.
- (48) Madhusoodhanan, S.; Sabbar, A.; Tran, H.; Lai, P.; Gonzalez, D.; Mantooth, A.; Yu, S.-Q.; Chen, Z. High-temperature analysis of optical coupling using AlGaAs/GaAs LEDs for high-density integrated power modules. *Sci. Rep.* **2022**, *12* (1), No. 3168.
- (49) Millea, M. F.; Kyser, D. Thermal decomposition of gallium arsenide. *J. Appl. Phys.* **1965**, *36* (1), 308–313.
- (50) Ram, R. J.; Dudley, J.; Bowers, J.; Yang, L.; Carey, K.; Rosner, S.; Nauka, K. GaAs to InP wafer fusion. *J. Appl. Phys.* **1995**, *78* (6), 4227–4237.

Supplementary Materials for
High-Temperature Strong Nonreciprocal Thermal Radiation from
Semiconductors

Bardia Nabavi¹, Sina Jafari Ghalekohneh¹, Komron J. Shayegan^{2,3}, Eric J. Tervo^{4,5},

Harry Atwater^{2,3}, and Bo Zhao^{1,*}

¹Department of Mechanical and Aerospace Engineering, University of Houston,
Houston, TX 77204, USA

²Thomas J. Watson Laboratory of Applied Physics, California Institute of Technology,
Pasadena, CA, 91125, USA

³Department of Electrical Engineering, California Institute of Technology,
Pasadena, CA, 91125, USA

⁴Department of Electrical and Computer Engineering, University of Wisconsin-Madison,
Madison, WI, 53706, USA

⁵ Department of Mechanical Engineering, University of Wisconsin-Madison,
Madison, WI, 53706, USA

*Corresponding author: bzhao8@uh.edu

Number of pages: 7

Number of figures: 2

Theoretical Model for GaAs

In the main text, we discuss the nonreciprocal radiative properties of doped InAs. The same procedure is applicable to other doped semiconductors including GaAs and its stoichiometric composition $\text{In}_x\text{Ga}_{1-x}\text{As}$, where x can range from 0 to 1. This section outlines the details of the model to calculate the nonreciprocal radiative properties of GaAs.

The temperature dependence of free carrier concentration of GaAs is mainly caused by the changes in the band gap and the effective density of states of both the conduction and valence bands:^{1,2}

$$E_g = E_{g0} - \frac{aT^2}{T+b}, \quad (\text{S1})$$

$$N_c = 8.63 \times 10^{13} T^{1.5} (1 - 1.931 \times 10^{-4} T - 4.19 \times 10^{-8} T^2 + 21e^{-\frac{E_{\Gamma L}}{2kT}} + 44e^{-\frac{E_{\Gamma X}}{2kT}}), \quad (\text{S2})$$

$$N_v = 1.83 \times 10^{15} T^{1.5} \quad (\text{S3})$$

where E_g is the band gap, E_{g0} , a , and b are empirical constants with values of 1.519 eV, 5.409×10^{-4} eV/K, and 204 K, respectively.^{1,2} N_c and N_v are the effective densities of states in the conduction and valence bands in cm⁻³, respectively. $E_{\Gamma L}$ and $E_{\Gamma X}$ represent the energy separation between Γ -L and Γ -X valleys in eV, respectively, and k is the Boltzmann constant. Carrier concentration (n) can be calculated using Eqs. (11) and (12) in the main article.

Subsequently, Eq. (13) in the main text can be applied to calculate the effective electron mass of GaAs as well as any binary or ternary semiconductor.^{3,4} We obtain the temperature effect on the electron scattering rate from a widely used empirical model for the mobility:⁵

$$\mu_{LF}(n,T) = \mu_{min} + \frac{\mu_{max} \left(\frac{380}{T} \right)^{\psi_1} - \mu_{min}}{1 + \left(\frac{n}{n_{ref} \left(\frac{T}{300} \right)^{\psi_2}} \right)^{\zeta}} \quad (\text{S4})$$

where n_{ref} is reference doping concentration as $6 \times 10^{16} \text{ cm}^{-3}$, μ_{\max} is the mobility at 300 K and μ_{\min} is the minimum mobility, which equal to 9400 and $500 \text{ cm}^2/\text{V}\cdot\text{s}$, respectively, for n -doped GaAs.⁵ ψ_1 , ψ_2 , and ζ are determined experimentally⁵ as 2.1, 3, and 0.394, respectively. Therefore, the scattering rate can be calculated using these empirical constants and Eq. (15).

Besides the parameters related to the free electrons, the high-frequency relative permittivity (ϵ_{∞}) also varies with temperature.^{6,7} Based on the tabulated data from Ref. 7, we derive a linear model using least-squares regression to capture this dependence:

$$\epsilon_{\infty} = \delta T + \sigma \quad (\text{S5})$$

where δ and σ are 0.0044 and 10.5583 for GaAs. As temperature rises, the high-frequency permittivity increases due to its linear dependence on this parameter, leading to a shift in the ENZ region of GaAs. Moreover, the effective electron mass for GaAs follows the general equation similar to InAs, as discussed in Eq. (13).

Theoretical Model for $\text{In}_{0.53}\text{Ga}_{0.47}\text{As}$

Since $\text{In}_x\text{Ga}_{1-x}\text{As}$ is a ternary alloy, its band parameters are more complex to determine.² For this calculation, x is chosen as 0.53. To simplify the calculation of the effective parameters that influence the dielectric function of $\text{In}_{0.53}\text{Ga}_{0.47}\text{As}$, Vegard's law⁸ is applied. This method divides the material as a mixture of GaAs and InAs, using a weighted average approach to determine its band parameters. For simplicity, parameter (y) is defined as $y = 1 - x$. Accordingly, the band gap of this material falls between the band gaps of InAs and GaAs:⁹⁻¹¹

$$E_g = 0.42 + 0.625y - \left(\frac{5.8}{T+300} - \frac{4.19}{T+271} \right) 10^{-4} T^2 y - \frac{4.19 \times 10^{-4} T^2}{(T+271)} + 0.475y^2 \quad (\text{S6})$$

$$N_c = 4.82 \times 10^{15} (0.023 + 0.037y + 0.003y^2)^{1.5} T^{1.5} \quad (\text{S7})$$

$$N_v = 4.82 \times 10^{15} (0.41 - 0.1y)^{1.5} T^{1.5} \quad (\text{S8})$$

Similarly, carrier concentration can be calculated using Eqs. (11) and (12). Additionally, Vegard's law is applied to calculate the effective electron mass:^{3,8}

$$m_{\text{In}_x\text{Ga}_{1-x}\text{As}}^* = xm_{\text{InAs}}^* + ym_{\text{GaAs}}^* \quad (\text{S9})$$

High-frequency permittivity is also calculated by applying Vegard's law⁸ based on the high-frequency permittivity values obtained for InAs and GaAs in Eqs. (16) and (S5):^{6,8,10}

$$\varepsilon_{\infty} = x\varepsilon_{\infty_{\text{InAs}}} + y\varepsilon_{\infty_{\text{GaAs}}} \quad (\text{S10})$$

Carrier concentration (n), electron effective mass (m^*), band gap (E_g), and scattering rate of carriers (γ) are temperature-dependent. This characteristic induces the change of plasma frequency (ω_p) and cyclotron frequency (ω_c) as shown in Fig. S1. As a result, the values of diagonal and off-diagonal terms in the permittivity tensor change. Since off diagonal term directly affects the nonreciprocity of the material through the cyclotron motion of carriers¹²⁻¹⁴, any change in this parameter leads to a significant change in the contrast between absorptivity and emissivity, highlighting radiative nonreciprocity.

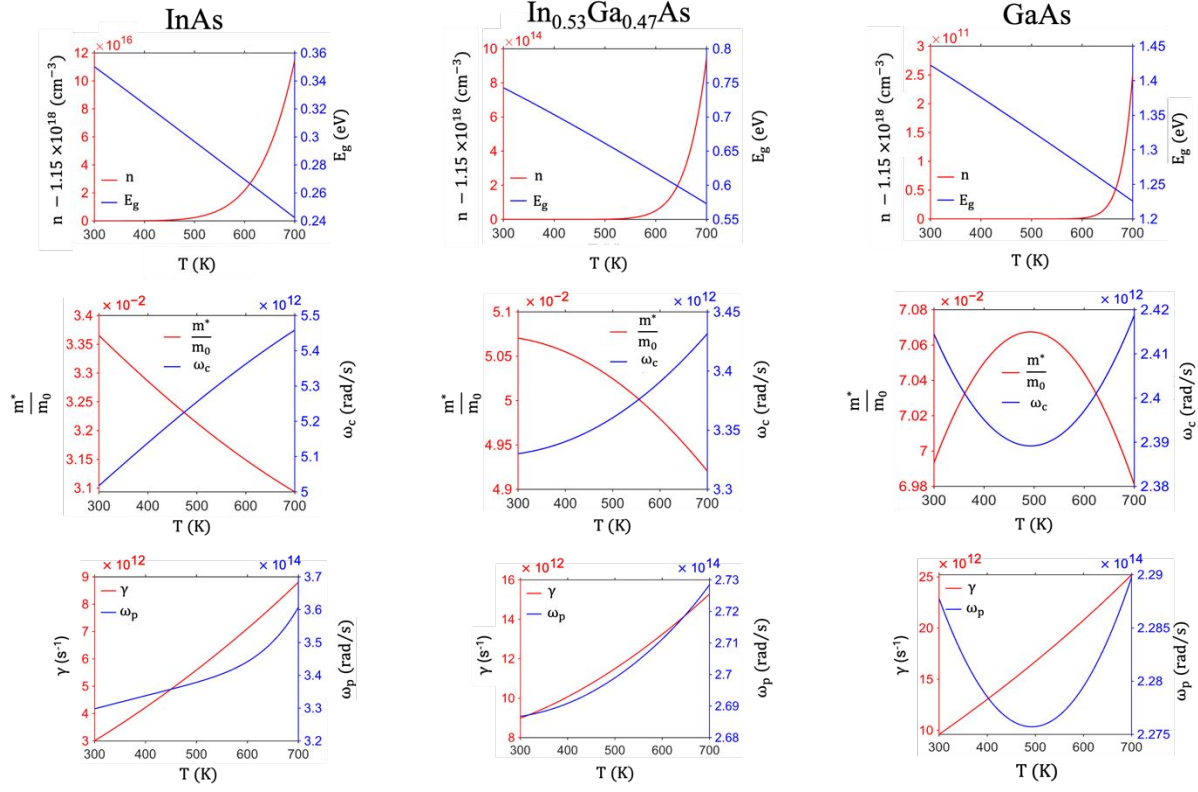


Figure S1. Band parameters and electron mobility as a function of temperature for InAs, In_{0.53}Ga_{0.47}As, and GaAs. As temperature increases, the band gap decreases due to thermal lattice expansion. Beyond 500-700 K, carrier concentration increases noticeably, indicating that the freeze-out region no longer occurs.⁹ As the band gap increases from InAs to GaAs, the freeze-out region decreases. Consequently, the plasma frequency changes due to variation in carrier concentration. The effective electron mass varies with temperature according to a polynomial relationship.^{3,4} This variation leads to quadratic dependence of the cyclotron frequency on temperature. Additionally, the scattering rate increases with temperature, influenced by low-field mobility of electron.⁵

Angular Dependence of the Nonreciprocal Behavior

Nonreciprocal contrast is enhanced at wider angles of incident. A numerical investigation is conducted for different materials. The temperatures of a single-layer structure of InAs, $\text{In}_{0.53}\text{Ga}_{0.47}\text{As}$, and GaAs are set at 600 K while applying an external magnetic field of 1 T in z -direction. It is assumed that each material has the same doping level of $3.24 \times 10^{18} \text{ cm}^{-3}$ and a thickness of 525 μm . As illustrated in Fig. S2, even at high temperatures, strong contrasts (~ 0.2) can be observed at more oblique directions. Since InAs has the lowest band gap compared to the other two other materials¹⁵, ENZ occurs at shorter wavelengths (12.5 μm).^{2,16} The Brewster modes of $\text{In}_{0.53}\text{Ga}_{0.47}\text{As}$ and GaAs are 15 μm and 17 μm , respectively, and the contrast between absorptivity and emissivity reduces as temperature increases.

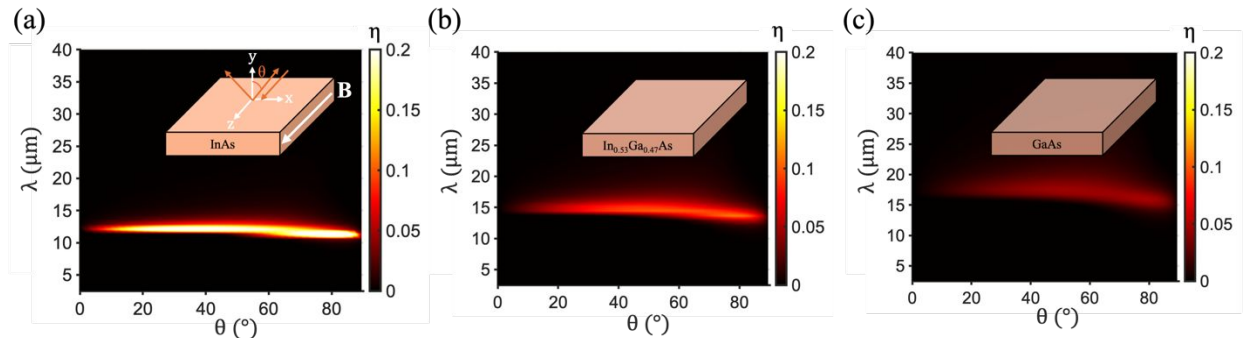


Figure S2. Contrast (η) contour in contrast to wavelength (λ) and angle of incidence (θ).

References

- (1) Varshni, Y. P. Temperature dependence of the energy gap in semiconductors. *Physica D: Nonlinear Phenomena* **1967**, *34*, 149-154.
- (2) Levinshtein, M. Handbook series on semiconductor parameters. *World Scientific* **1997**. doi.org/10.1142/2046
- (3) Bouarissa, N.; Aourag, H. Effective masses of electrons and heavy holes in InAs, InSb, GaSb, GaAs and some of their ternary compounds. *Infrared Physics and Technology* **1999**, *40*, 343-349.
- (4) Nakwaski, W. Effective masses of electrons and heavy holes in GaAs, InAs, AlAs and their ternary compounds. *Physica B: Condensed Matter* **1995**, *210* (1), 1-25.
- (5) Sotoodeh, M.; Khalid, A.; Rezazadeh, A. Empirical low-field mobility model for III-V compounds applicable in device simulation codes. *Journal of Applied Physics* **2000**, *87* (6), 2890-2900.
- (6) Degheidy, A. R.; Elkenany, E. B.; Madkour, M. A. K.; AbuAli, A. M. Temperature dependence of phonons and related crystal properties in InAs, InP and InSb zinc-blende binary compounds. *Computational Condensed Matter* **2018**, *16*, e00308. doi.org/10.1016/j.cocom.2018.e00308
- (7) Strzalkowski, I.; Joshi, S.; Crowell, C. Dielectric constant and its temperature dependence for GaAs, CdTe, and ZnSe. *Applied Physics Letters* **1976**, *28* (6), 350-352.
- (8) Vegard, L. Die konstitution der mischkristalle und die raumfüllung der atome. *Zeitschrift für Physik* **1921**, *5* (1), 17-26.
- (9) Pierret, R. F. Semiconductor Device Fundamentals. *Addison-Wesley Publishing Company* **1996**. 1-69.
- (10) Moore, W. J.; Holm, R. T. Infrared dielectric constant of gallium arsenide. *Journal of Applied Physics* **1996**, *80* (12), 6939-6942.
- (11) Paul, S.; Roy, J. B.; Basu, P. K. Empirical expressions for the alloy composition and temperature dependence of the band gap and intrinsic carrier density in $\text{Ga}_x\text{In}_{1-x}\text{As}$. *Journal of Applied Physics* **1991**, *69* (2), 827-829.
- (12) Zhu, L.; Fan, S. Near-complete violation of detailed balance in thermal radiation. *Physical Review B* **2014**, *90* (22), 220301.
- (13) Madelung, O. Semiconductors: data handbook. *Springer Science & Business Media* **2004**. 397-419.
- (14) Zhao, B.; Shi, Y.; Wang, J.; Zhao, Z.; Zhao, N.; Fan, S. Near-complete violation of Kirchhoff's law of thermal radiation with a 0.3T magnetic field. *Optics Letters* **2019**, *44* (17), 4203-4206.
- (15) Sze, S. M. Semiconductor devices: physics and technology. *John Wiley & Sons* **2008**. 43-77.
- (16) Shayegan, K. J.; Biswas, S.; Zhao, B.; Fan, S.; Atwater, H. A. Direct observation of the violation of Kirchhoff's law of thermal radiation. *Nature Photonics* **2023**, *17* (10), 891-896.